

Optically driven oscillations of ellipsoidal particles. Part II: Ray-optics calculations

J.-C. Loudet^a, B.M. Mihiretie^b, and B. Pouliquen

Université de Bordeaux, CNRS, Centre de Recherche Paul Pascal, Avenue A. Schweitzer, F-33600 Pessac, France

Received 15 July 2014 and Received in final form 21 October 2014

Published online: 22 December 2014 – © EDP Sciences / Società Italiana di Fisica / Springer-Verlag 2014

Abstract. We report numerical calculations on the mechanical effects of light on micrometer-sized dielectric ellipsoids immersed in water. We used a simple two-dimensional ray-optics model to compute the radiation pressure forces and torques exerted on the object as a function of position and orientation within the laser beam. Integration of the equations of motion, written in the Stokes limit, yields the particle dynamics that we investigated for different aspect ratios k . Whether the beam is collimated or focused, the results show that above a critical aspect ratio k_C , the ellipsoids cannot be stably trapped on the beam axis; the particle never comes to rest and rather oscillates permanently in a back-and-forth motion involving both translation and rotation in the vicinity of the beam. Such oscillations are a direct evidence of the non-conservative character of optical forces. Conversely, stable trapping can be achieved for $k < k_C$ with the particle standing idle in a vertical position. These predictions are in very good qualitative agreement with experimental observations. The physical origin of the instability may be understood from the force and torque fields whose structures greatly depend on the ellipsoid aspect ratio and beam diameter. The oscillations arise from a non-linear coupling of the forces and torques and the torque amplitude was identified as the bifurcation control parameter. Interestingly, simulations predict that sustained oscillations can be suppressed through the use of two coaxial counterpropagating beams, which may be of interest whenever a static equilibrium is required as in basic force and torque measurements or technological applications.

1 Introduction

That light can exert forces on material objects has been known for more than a century [1, 2]. Momentum transfer from photons to matter results in physical motion and this can be most easily evidenced with lasers at the mesoscopic scale of biological cells [3–6] and down to atoms (laser cooling) [7–9]. Radiation pressure (RP) forces exerted on solid bodies is the main subject of the present article, which is a follow up work of a Part I paper [10] dedicated to an experimental investigation of the mechanical effects of light on non-spherical microparticles. Here, we rather focus on numerical simulations.

Our interest in the field was initially fueled by the surprising optical levitation properties of elongated (prolate) micrometer-sized dielectric ellipsoids [11, 12]. In those experiments, the ellipsoids were immersed in water and we used an optical levitator (OL) made of a moderately focused laser beam to characterize the mechanical response of the illuminated particle. Unlike the widespread optical tweezers (OT) [4], OL only provides a 2-dimensional (2d)

trap but a wealth of useful information can already be extracted in this simple geometry which allows long-working distances. Our results show that, while “short” ellipsoids can be radially trapped and lifted up with no surprise, similarly to spheres, longer ellipsoids behave quite differently: such particles cannot be radially trapped during ascension and rather undergo a back-and-forth motion in and out of the beam involving both translations and rotations. Increasing the laser power makes the particle tumble faster, leading to light-driven sustained oscillations. Understanding this “particle dance”, the matter of our work, is a problem of general interest in the frame of optical manipulation of particles with arbitrary shapes, which is much less mastered than that of spheres [13–15].

As pointed out in [10], other observations of “dancing particles” have been previously reported with micro-rods [13, 16], nano-fibers [17] or disks [18, 19] held in optical tweezers. However, no formal interpretation of the phenomena was provided as far as we know¹. On the theoretical and numerical sides, a bunch of studies dealt with the trapping properties of rods [20, 21], cylinders [22–25], prolate and oblate ellipsoids [26–29]. Both attraction and

^a e-mail: loudet@crpp-bordeaux.cnrs.fr

^b Present address: Department of Physics, University of Gothenburg, Sweden.

¹ The model worked out in [19] is irrelevant to our situation; see [10, 11].

repulsion from the laser beam are predicted, as shortly reviewed in [10]. The important point is that, in addition to shape dependence, both the location and orientation of the particle within the beam greatly alter its response to the incoming laser light. Non-zero optical torques occur, even for particles made of a homogeneous isotropic non-absorbing material illuminated by linearly polarized beams.

However, none of the available computations has predicted the kind of oscillations we encountered with ellipsoids in bulk water [11, 12]. In [11] we showed that simple simulations based on a 2-dimensional ray-optics model of the ellipsoid-laser beam interaction were successful in capturing the main trends of the particle dynamics. Thus, RP forces alone can account for the observed oscillations. Following the same approach, the purpose of this paper is to provide additional results and make new qualitative predictions. Of primary importance is the influence of the beam divergence on the onset of oscillations. An important point which was not explored in [11] is the influence of beam diffraction on the existence of oscillations. Only a collimated beam, *i.e.* a set of parallel rays was assumed in [11]. However the laser beam used in experiments was focused down to $1.3\ \mu\text{m}$ in beam waist radius, meaning that beam diffraction was significant on the scale of the particle size (the Rayleigh length, about $15\ \mu\text{m}$, was comparable to the ellipsoid major axis). We then cannot ignore beam divergence as another control parameter in determining the particle dynamical response. Introducing beam diffraction effects into a ray-optics simulation is not straightforward, but, at least, we may test the influence of the finite beam divergence using a set of rays with an aperture comparable to that of the actual laser beam, in the far field. In this way, the simulation gives a hint about the effect of more or less focusing the actual laser beam, *i.e.* of varying its beam waist. We also explore the possibility of getting rid of these oscillations through the addition of a second counterpropagating beam, which could be useful from a technological viewpoint. Indeed, the occurrence of oscillations is a major drawback towards the design of laser-assisted assembled microstructures which require precise positioning and orientation of particles such as nanowires, nanotubes, graphene or quantum dots [16, 17, 30, 31].

The outline of the paper is as follows: in sect. 2, we present the details of our calculations based on a 2-dimensional ray-optics model of the RP forces and torques exerted on a prolate ellipsoid. The numerical results are reported in sect. 3 for both a collimated and a focused laser beam. We provide detailed force and torque maps in the parameter space. These maps turn out to be very valuable in unraveling the physical origin of the aforementioned sustained oscillations. State diagrams are computed to summarize the various dynamical states of the particle as a function of its aspect ratio and position inside the beam. Section 4 deals with preliminary results obtained in the presence of a second counterpropagating beam. Depending on the respective powers of the beams, sustained oscillations are predicted to disappear. A dis-

cussion and conclusion close the paper along with some prospects.

2 Model

The goal of this part is to set up a simulation of the ellipsoidal particles' oscillations using a very simple optical model based on ray-optics [32]. Our approach is restricted to 2 dimensions which, as we shall see below, turns out to be good enough to account for the main experimental facts.

To simulate the particle's response, we must first compute the optical force \mathbf{F} and torque $\boldsymbol{\Gamma}$ acting on the particle in a laser beam of given characteristics. In a rigorous version, the problem amounts to calculating the electromagnetic (e.m.) field scattered by the particle. In theory, \mathbf{F} and $\boldsymbol{\Gamma}$ can then be obtained from the Maxwell stress tensor of the whole e.m. field (incident+scattered) by integration over the whole surface that surrounds the object [14, 33].

When the particle is not more than a few micrometers in size, the wave nature of the e.m. field must be taken into account. The case of a sphere that scatters light from a focused laser beam has been the matter of numerous dedicated works since the eighties. Rigorous solutions to this problem have been obtained and are known as "Generalized Lorenz-Mie Theory" (GLMT) [34, 35]. The GLMT has been extended to spheroidal shapes (*i.e.* cylindrically symmetrical ellipsoids) by Xu *et al.* [36] and for particle aspect ratios (k) up to 1.5.

In general, calculation of the scattered field by particles of more complicated shapes is a very difficult task that can only be performed using numerical techniques. Different methods have been proposed to handle about any particle shape, namely the discrete dipole approximation (DDA) [25, 27, 37–40], the finite difference time domain (FDTD) [41, 42], the vector finite element [43], multi-level multipole [44, 45], and T-matrix methods [46, 47].

Calculating the field scattered by our ellipsoidal particles, of large aspect ratio and more than $10\ \mu\text{m}$ in size, is currently at the limit of possibilities of existing numerical methods. As aforesaid, we thus opted for a very simplified analysis based on ray-optics (RO) in two dimensions. The assumptions made in the model are rough, meaning that the simulation has no pretension to be quantitatively accurate. In spite of these limitations, we will see that the model yet captures the main trends of the particle's mechanical response to the laser beam.

2.1 Radiation pressure force and torque

In the RO regime, we assume that the laser beam ($\lambda_0 = 514.5\ \text{nm}$, total power P_T) consists of a bundle of individual rays (typically, a few thousands), propagating upwards in the z -direction. The intensity of rays, $I(\mathbf{r})$, at point $\mathbf{r} = x\hat{\mathbf{x}} + z\hat{\mathbf{z}}$ of a 2-dimensional Cartesian system of coordinates (x, z) with unit vectors $(\hat{\mathbf{x}}, \hat{\mathbf{z}})$, follows a Gaussian distribution along x . Since we only address the

problem in 2 dimensions, rays keep inside the same plane during propagation. In the first version of the model, we made the assumption of a collimated beam (parallel rays) which amounts to supposing that the laser beam structure is invariant along z . But this is not exactly so in the experiments because the beam waist ($2\omega_0 \approx 2.6 \mu\text{m}$) is small enough for diffraction to be visible on the scale of the particle size (the diffraction length, or Rayleigh range, is about $15 \mu\text{m}$ while the ellipsoid long axis exceeds $20 \mu\text{m}$ for $k = 3$). Diffraction effects are not included in the RO model (by definition), but we may simulate a focused beam, over an aperture approximately equal to that of the real laser beam in the far field. The beam waist is located at $z = 0$ in the laboratory frame; the rays are emitted in the $z < 0$ region and they all converge towards the origin, *i.e.* the $(x = 0, z = 0)$ point. With no particle in the beam path, all rays pass through the origin and continue their propagation in straight lines in the $z > 0$ region. The beam radius $\omega(z)$ of the $1/e^2$ irradiance contour, after the wave has propagated a distance z , is assumed to be given by $\omega(z) = \theta_D z$, where θ_D is the beam divergence which is supposed to be small ($\theta_D \ll \pi/2$). We may then define a parameter ω_0 such that $\theta_D = \lambda/\pi\omega_0$, where ω_0 represents the beam waist of an actual Gaussian laser beam which, in the far field, has the same divergence as that of our model laser beam. The far-field condition holds for $z \gg z_R = \pi\omega_0^2/\lambda$, where z_R is called the Rayleigh range. The power P_i of the i -th ray of our model Gaussian beam at a given point \mathbf{r} is given by

$$P_i = I(\mathbf{r})\Delta A = \frac{2P_T}{\pi\omega^2(z)} \exp\left[-\frac{2r^2}{\omega^2(z)}\right] \Delta A, \quad (1)$$

where ΔA is the projection, in the xy plane, of the infinitesimal surface ΔS illuminated by the ray on the particle surface at the incident point. In our 2d approach, ΔA simply amounts to the beam sampling spacing Δx in the x -direction. In the case of a collimated beam, $\omega(z)$ is constant and equals ω_0 .

The procedure we used to compute the RP forces and torques is quite similar to that described in detail in refs. [28, 48–51]. The ellipsoidal particle is assumed to be made of a homogeneous, isotropic and non-absorbing material. Each incident ray becomes multiply reflected and refracted along the ellipsoid's boundary, each time transferring momentum between the ray and the particle. Each scattering event j therefore contributes an elementary force \mathbf{f}_j . From fig. 1 we see that, for the initial ray strike ($j = 0$)

$$\mathbf{f}_0 = \frac{n_1 P}{c} \left(\hat{\mathbf{i}}_0 - R_0 \hat{\mathbf{r}}_0 - n_{21} T_0 \hat{\mathbf{t}}_0 \right), \quad (2)$$

whereas for the successive ray strikes ($j \geq 1$)

$$\begin{aligned} \mathbf{f}_j &= \frac{n_1 P}{c} T_0 \left[n_{21} \left(\prod_{k=1}^{j-1} R_k \right) \hat{\mathbf{i}}_j - \left(\prod_{k=1}^{j-1} R_k \right) T_j \hat{\mathbf{t}}_j \right. \\ &\quad \left. - n_{21} \left(\prod_{k=1}^j R_k \right) \hat{\mathbf{r}}_j \right], \end{aligned} \quad (3)$$

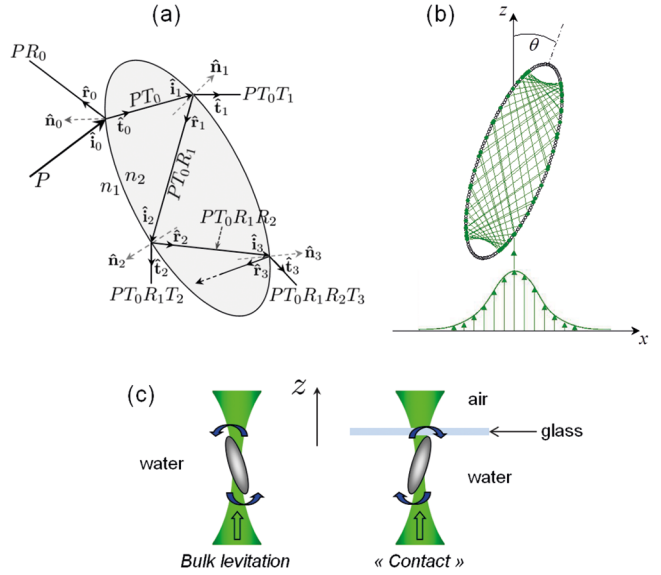


Fig. 1. (a) Schematic of the 2d ray-optics (RO) model used to compute the radiation pressure force due the scattering of a single incident ray of power P by a dielectric prolate ellipsoid. A few reflected, refracted and transmitted rays are shown for illustration (see text for the definition of symbols). (b) The ellipsoid's long axis makes an angle θ with respect to the z -axis. 60 reflections inside the ellipsoid are shown here for illustration. The laser beam has a Gaussian intensity profile along x . (c) Two different levitation geometries used in experiments [11, 12]: in bulk water (left panel) or in contact to the top glass of the sample chamber (right panel). The arrows indicate the oscillatory behavior of the ellipsoid if $k > k_C$ (see text).

where $\hat{\mathbf{i}}_j$, $\hat{\mathbf{r}}_j$, $\hat{\mathbf{t}}_j$ are unit vectors denoting, respectively, the incident, reflected and transmitted ray's directions at boundary points M_j . c is the speed of light in vacuum and n_1 , n_2 (with $n_{21} = n_2/n_1$) are the refractive indices in the continuous (external) medium and inside the particles, respectively. R_j , T_j denote the Fresnel power reflectance and transmittance and P is the power of the initial incoming ray. Since $\hat{\mathbf{r}}_j = \hat{\mathbf{i}}_{j+1}$ for all $j \geq 1$, the force \mathbf{f} exerted by a *single* ray on the particle is obtained by vector summation of all scattering events and may be put into the form

$$\mathbf{f} = \frac{n_1 P}{c} \mathbf{q}, \quad \text{with} \quad \mathbf{q} = \hat{\mathbf{i}}_0 - R_0 \hat{\mathbf{r}}_0 - T_0 \sum_{j=1}^{\infty} T_j \left(\prod_{k=1}^{j-1} R_k \right) \hat{\mathbf{t}}_j. \quad (4)$$

The modulus of the dimensionless vector \mathbf{q} is often called the “trapping efficiency of the ray”. The elementary force \mathbf{f}_j (eqs. (2), (3)) contributes an elementary torque $\boldsymbol{\tau}_j = \mathbf{r}_j \times \mathbf{f}_j$, where \mathbf{r}_j is the vector joining the ellipsoid center C , taken as the reference point, to the impact point M_j . The torque due to a *single* ray is then simply given by

$$\boldsymbol{\tau} = \sum_{j=0}^{\infty} \boldsymbol{\tau}_j. \quad (5)$$

The unit vectors $\hat{\mathbf{i}}_j$, $\hat{\mathbf{r}}_j$, $\hat{\mathbf{t}}_j$ are found using the classical laws of reflection and refraction given by the Fresnel equations.

For the initial ray strike ($j = 0$), we have

$$\hat{\mathbf{r}}_0 = \hat{\mathbf{i}}_0 + 2c_0\hat{\mathbf{n}}_0,$$

$$\hat{\mathbf{t}}_0 = n_{12}\hat{\mathbf{i}}_0 + \left[n_{12}c_0 - \sqrt{1 + n_{12}^2(c_0^2 - 1)} \right] \hat{\mathbf{n}}_0,$$

where $c_0 = -\hat{\mathbf{i}}_0 \cdot \hat{\mathbf{n}}_0$ and $n_{12} = n_1/n_2$. For $j \geq 1$, the above relations change to

$$\hat{\mathbf{r}}_j = \hat{\mathbf{i}}_j - 2c_j\hat{\mathbf{n}}_j,$$

$$\hat{\mathbf{t}}_j = n_{21}\hat{\mathbf{i}}_j + \left[-n_{21}c_j + \sqrt{1 + n_{21}^2(c_j^2 - 1)} \right] \hat{\mathbf{n}}_j,$$

with $c_j = \hat{\mathbf{i}}_j \cdot \hat{\mathbf{n}}_j$. As the Fresnel coefficients R_j , T_j depend on polarization, we suppose that the beam is linearly polarized either along $\hat{\mathbf{x}}$ (S mode) or $\hat{\mathbf{y}} = \hat{\mathbf{z}} \times \hat{\mathbf{x}}$ (P mode). In such cases, R_j and T_j are given by

$$R_j^S = \left| \frac{n_{21}(\hat{\mathbf{i}}_j \cdot \hat{\mathbf{n}}_j) - (\hat{\mathbf{t}}_j \cdot \hat{\mathbf{n}}_j)}{n_{21}(\hat{\mathbf{i}}_j \cdot \hat{\mathbf{n}}_j) + (\hat{\mathbf{t}}_j \cdot \hat{\mathbf{n}}_j)} \right|^2,$$

$$R_j^P = \left| \frac{(\hat{\mathbf{i}}_j \cdot \hat{\mathbf{n}}_j) - n_{21}(\hat{\mathbf{t}}_j \cdot \hat{\mathbf{n}}_j)}{(\hat{\mathbf{i}}_j \cdot \hat{\mathbf{n}}_j) + n_{21}(\hat{\mathbf{t}}_j \cdot \hat{\mathbf{n}}_j)} \right|^2,$$

with $T_j^S = 1 - R_j^S$ and $T_j^P = 1 - R_j^P$. In contrast to spheres, when a ray enters an ellipsoid, total internal reflection may occur if the incident angle α exceeds the critical angle $\alpha_c = \arcsin(n_{12})$. Hence, we have

$$R_j = \begin{cases} R_j^S & \text{or } R_j^P \quad \text{if } \alpha_j \leq \alpha_c, \\ 1 & \quad \quad \quad \text{if } \alpha_j > \alpha_c, \end{cases}$$

$$T_j = \begin{cases} 1 - R_j & \text{if } \alpha_j \leq \alpha_c, \\ 0 & \quad \quad \quad \text{if } \alpha_j > \alpha_c. \end{cases}$$

We keep track of the propagation of a given ray inside the ellipsoid using a standard ray-tracing technique [32] and stop the propagation when the ray's power has decreased by a factor of about 10^3 ($\approx 0.1\%$ of the initial ray's power remains) [49]. We checked that pushing the computation further (*i.e.* with a factor greater than 10^3) did not significantly change the final values of \mathbf{f} (eq. (4)) and $\boldsymbol{\tau}$ (eq. (5)).

The total net force \mathbf{F} acting on the ellipsoid is calculated by summing the contributions of the individual rays that hit the particle surface, *i.e.* $\mathbf{F} = \sum_i^{N_r} \mathbf{f}_i = \frac{n_1}{c} \sum_i^{N_r} P_i \mathbf{q}_i$, where N_r is the number of rays impinging on the particle, P_i (eq. (1)) and \mathbf{q}_i (eq. (4)) are the power and trapping efficiency vector of the i -th ray, respectively. Similarly, the net torque $\boldsymbol{\Gamma}$ acting about the center of mass of the ellipsoid is computed by adding the individual torques due to each ray (eq. (5)), namely $\boldsymbol{\Gamma} = \sum_i^{N_r} \boldsymbol{\tau}_i$.

The calculation of \mathbf{F} and $\boldsymbol{\Gamma}$ is worked out for various positions x , z and tilt angles θ of the ellipsoid, $|x| \leq x_{\max}$, $|\theta| \leq \theta_{\max}$, with a corresponding (121×36) resolution. Note that these computations are not restricted to small excursions, meaning that the ellipsoid may move almost

completely out of the beam, as observed in the experiments. We thus obtain maps of \mathbf{F} and $\boldsymbol{\Gamma}$ for different configurations of the ellipsoid with respect to the laser beam. Some examples of such maps will be provided below.

2.2 Hydrodynamic friction force and torque—equations of motion

In addition to RP forces and torques, the particle immersed in water also experiences gravity and hydrodynamic friction forces and torques, both in translation (\mathbf{F}_{Hx}) and rotation ($\boldsymbol{\Gamma}_{H\theta}$). Gravity intervenes through the particle weight, corrected for buoyancy: $\tilde{m}g$. Inertia forces and torques are negligible in the experiments reported in [10]. This can be checked by estimating the particle Reynolds number $Re = \rho U a / \eta$, with $\rho = 1.05 \text{ g cm}^{-3}$ (the density of polystyrene latex) and $\eta \cong 1 \text{ mPa s}$ (the water viscosity at room temperature). a is the ellipsoid semi-long axis and U is the typical velocity of the oscillating ellipsoid which we estimate through $U \approx a\nu$, where ν is the frequency of oscillation. Taking $a = 15 \mu\text{m}$ and $\nu \leq 5 \text{ Hz}$, we get $Re \approx 10^{-3}$. Thus, to a first approximation, \mathbf{F}_{Hx} and $\boldsymbol{\Gamma}_{H\theta}$ reduce to their Stokes limit

$$\mathbf{F}_{Hx} = -\gamma_x \dot{x} \hat{\mathbf{x}}, \quad (6)$$

$$\boldsymbol{\Gamma}_{H\theta} = \gamma_\theta \dot{\theta} \hat{\mathbf{y}}, \quad (7)$$

where γ_x , γ_θ are the friction coefficients for the motion of the ellipsoid in translation along $\hat{\mathbf{x}}$ and in rotation around $\hat{\mathbf{y}}$, respectively. The dot means time derivative and θ is the particle tilt angle with respect to the vertical axis (see fig. 1b). In the above equations, we supposed that translational and rotational friction were decoupled.

We obtain the equations for particle motion by writing that the total force and torque (RP + weight + hydrodynamics) acting on the particle are null. Here, we give the simplified form of the equations, which holds in the limit of small tilt angle ($\theta \ll \pi/2$) (set 1)

$$\mathbf{F} \cdot \hat{\mathbf{x}} = \gamma_x \dot{x}, \quad (8)$$

$$\mathbf{F} \cdot \hat{\mathbf{z}} = \tilde{m}g + \gamma_z \dot{z}, \quad (9)$$

$$\boldsymbol{\Gamma} \cdot \hat{\mathbf{y}} = -\gamma_\theta \dot{\theta}, \quad (10)$$

where γ_z is the friction coefficient for a translational motion along $\hat{\mathbf{z}}$. $\dot{\theta}$ is conventionally taken > 0 when the particle rotates counterclockwise. Due to the minus sign in eq. (10), a positive torque makes the particle rotate clockwise. After integration, eqs. (8)-(10) describe the ellipsoid motion in bulk water away from any boundaries. However, experimentally, it turned out much more convenient to observe the particle dynamics when it was lifted up to the top glass of the sample chamber [11, 12]. In such a configuration, which we refer to as “contact”, the ellipsoid center of mass remains at approximately constant altitude. We may model this particular situation through the addition of a contact force, \mathbf{F}_c , exerted on the chamber ceiling. Assuming that the contact condition does not significantly alter the hydrodynamic friction, \mathbf{F}_c is simply

vertical and given by $\mathbf{F}_c = F_z \hat{\mathbf{z}}$, where $F_z = \mathbf{F} \cdot \hat{\mathbf{z}}$ is the vertical component of the RP force. As already pointed out, the presence of the water-glass interface has no direct influence on the particle dynamical behavior. Indeed, in the experiments, the oscillations are general, be the ellipsoid located in the bulk or in contact to a solid or soft boundary [11, 12]. Therefore, the model should be able to reveal oscillations, even if hydrodynamic effects related to the proximity of a boundary are ignored. A specific lubrication term such as that elaborated in [19] may well play a role but is not essential in the model. In the contact configuration, eqs. (8)-(10) change to (set 2)

$$\mathbf{F} \cdot \hat{\mathbf{x}} = \gamma_x \dot{x}, \quad (11)$$

$$\Gamma \cdot \hat{\mathbf{y}} + \tilde{R} \theta \mathbf{F} \cdot \hat{\mathbf{z}} = -\gamma_\theta \dot{\theta}, \quad (12)$$

where \tilde{R} is a length given by $\tilde{R} = R k^{-4/3} (k^2 - 1)$ (see appendix A for its derivation). The second term on the l.h.s. of eq. (12) is a new term due to the torque exerted by the contact force (\mathbf{F}_c) when the ellipsoid tip is in contact to the top surface. This term is not essential for the onset of oscillations and we leave it there for the sake of completeness.

As we needed values for the friction coefficients ($\gamma_x, \gamma_z, \gamma_\theta$), we adopted those derived for prolate ellipsoids in 3d. A standard formulation reads: $\gamma_x = 6\pi\eta b G_b$, $\gamma_z = 6\pi\eta a G_a$ and $\gamma_\theta = 6\eta V G_\theta$. Here V is the ellipsoid volume, η is the water viscosity ($\cong 1 \text{ mPa s}$ at room temperature), b is the ellipsoid semi-short axis, while G_a, G_b, G_θ are geometrical factors which depend only on the aspect ratio $k (= a/b)$; they all increase with k and explicit expressions, derived from Perrin's equations, can be found in [52, 53]. Note that V is constant in our problem, since this is the volume of the mother sphere from which the ellipsoids are derived ($V \cong 524 \mu\text{m}^3$ for a sphere of radius $R = 5 \mu\text{m}$).

Although we will primarily focus on prolate ellipsoids ($k > 1$) hereafter, note that the 2-dimensional representation can also address the case of oblate ellipsoids ($k < 1$) through the $k \rightarrow 1/k$ transformation. However, it cannot deal of course with non-axisymmetric particles for which the third dimension is required.

Prior to computations, the above equations were non-dimensionalized using the following characteristic quantities: the length scale is set by the radius R of the mother sphere whereas the force scale is set by $F_0 = P_T/c$, where P_T is the total beam power. The time scale is defined by $t' = \eta R^2/F_0$, which corresponds to the characteristic time for the mother sphere to be trapped in on-axis configuration, within a numerical factor. Hence, we used the following dimensionless variables: $F_x^* = F_x/F_0$, $F_g^* = \tilde{m}g/F_0$, $\Gamma_y^* = \Gamma_y/(F_0 R)$, $t^* = t/t'$, $x^* = x/R$, $z^* = z/R$, $\gamma_x^* = \gamma_x/(\eta R)$, $\gamma_z^* = \gamma_z/(\eta R)$ and $\gamma_\theta^* = \gamma_\theta/(\eta R^3)$. Note that F_x^*, Γ_y^* do not depend on P_T for they are only functions of (x^*, z^*, θ, k) whereas $F_g^* \propto P_T^{-1}$. Depending on the considered situation, we numerically integrated either eqs. (8)-(10) (set 1) or eqs. (11), (12) (set 2), in dimensionless forms, using a standard fourth-order Runge-Kutta algorithm with a variable step size and error control [54, 55].

Results of integrations will be displayed hereafter for different k values.

3 Results

We will first consider a collimated laser beam, as in [11, 12], and present additional results under this assumption. We shall next address the case of a focused beam, which no longer makes the system z -invariant, as aforementioned.

3.1 Collimated beam

Unless otherwise specified, we assume the ellipsoid to be in the contact configuration defined in subsect. 2.2 (see also fig. 1c). As aforesaid, this situation is not restrictive as it does not change the results qualitatively.

Previous work showed that integration of eqs. (11), (12) lead to a sub-critical Hopf bifurcation between static and oscillating states above a well-defined k_C value [11, 12]. The simulation successfully reproduces the basic experimental trends for it shows that short ellipsoids ($k < k_C$) are stably trapped on the beam axis in a vertical position while longer ones ($k > k_C$) permanently oscillate in a periodic manner. In the former case, the origin $(0, 0)$ attracts all trajectories and is the only stable attractor in the computed two-dimensional dissipative phase space (x, θ) . Depending on k , it may either consist of a node or a focus (case of damped oscillations). For $k > k_C$, two attractors coexist: the aforementioned point attractor at the origin and a limit cycle located away from it. For small translational or rotational excursions of the ellipsoid, the origin is still a stable equilibrium point whereas for large initial shift or tilt, the ellipsoid falls into the catchment region of the limit cycle and all phase trajectories converge towards it [11, 12]. The computed coexistence of attractors departs from the super-critical character of the experimental bifurcation but, given its simplicity, the simulation nevertheless captures the main trend.

Why does the ellipsoid oscillate? Obviously k is one of the key variables to play with, and furthermore, needless to say that the forces and torques exerted on the particle must depend on k . This is indeed illustrated by the color-coded contour graphs of fig. 2 where F_x and Γ_y have been plotted in the (x, θ) -plane for various k values. Figure 2 shows how the shape and location of regions with positive or negative F_x (fig. 2a) and Γ_y (fig. 2b) drastically evolve with k . Thus, the onset of oscillations at k_C appears to be linked to a peculiar structure of the forces and torques. As a striking trend, we note that when k is increased, the force does not vary much in amplitude while the torque strongly increases (see the color charts on the right of each panel). A fine inspection reveals that these maps do not differ much at threshold ($k_C \cong 4.085$) and just below it ($k = 4$); the main difference rather lies in the torque value, which is a bit higher at k_C . Hence, the torque amplitude seems to be the key parameter driving

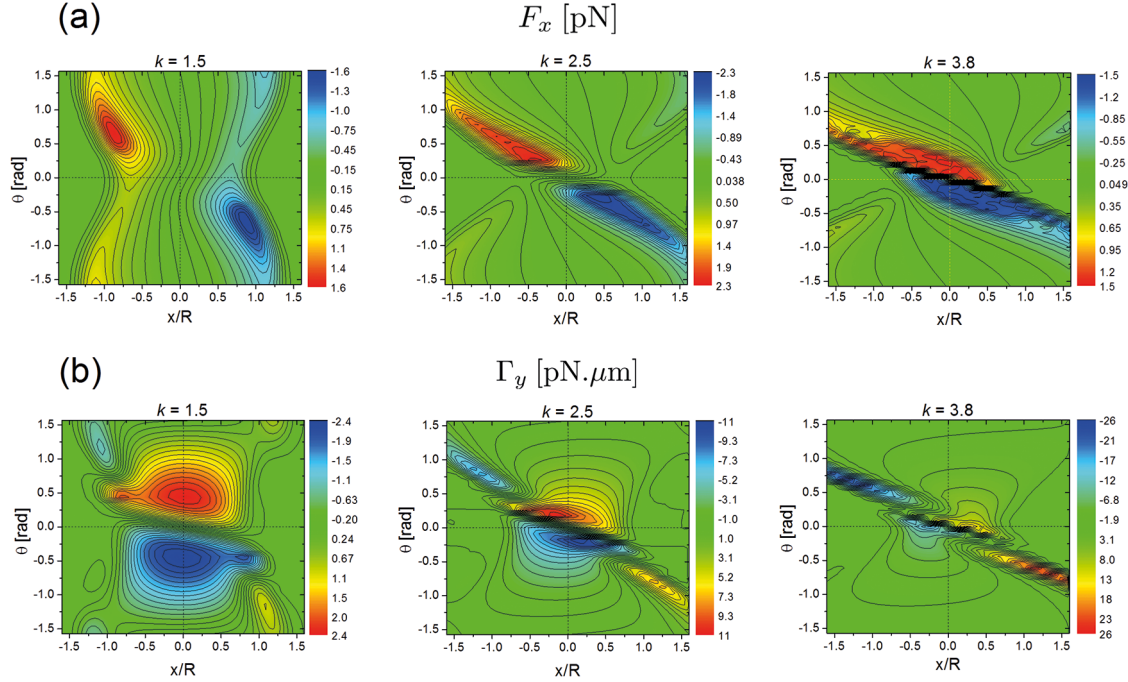


Fig. 2. Evolution of the computed force F_x (a) and torque Γ_y (b) maps as a function of k (beam radius $\omega_0 = 1.3 \mu\text{m}$, S polarization mode, collimated beam).

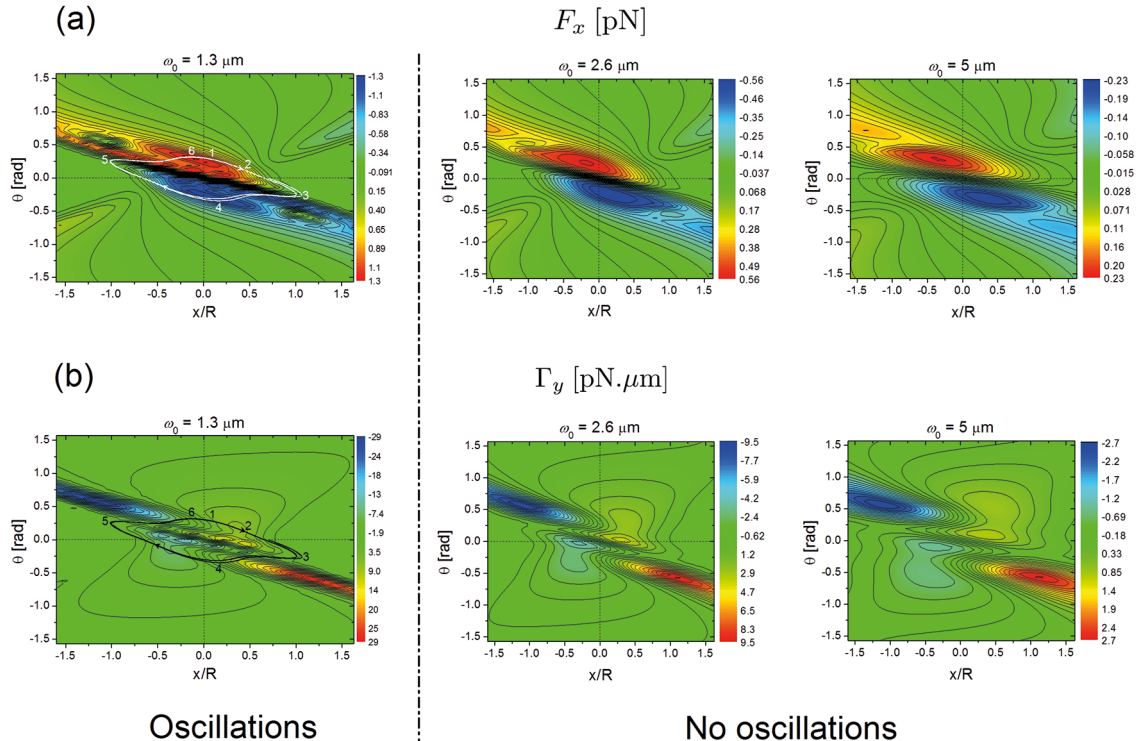


Fig. 3. Evolution of the computed force F_x (a) and torque Γ_y (b) maps as a function of beam radius ω_0 ($k = 4.1$, S polarization mode, collimated beam). Only for $\omega_0 = 1.3 \mu\text{m}$ do the displayed force and torque maps lead to sustained oscillations. The obtained limit cycle (in white for F_x and black for Γ_y) has been superimposed on the maps. The arrows indicate a clockwise cyclic motion while the digits refer to particular situations (see text for details).

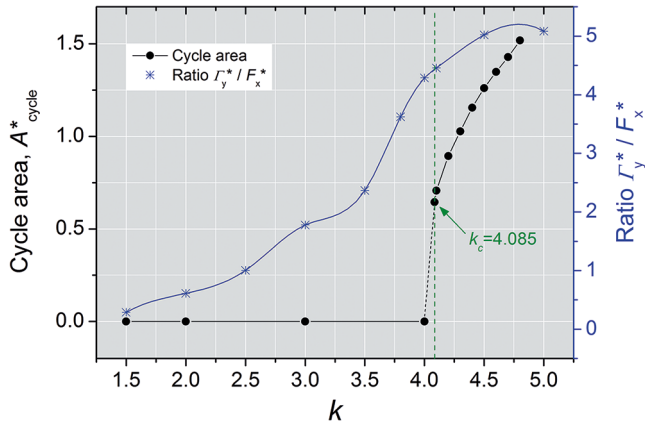


Fig. 4. Limit cycle area, A_{cycle}^* , force F_x^* and torque Γ_y^* as a function of the ellipsoid aspect ratio k (case of a collimated beam, S polarisation mode, beam waist $w_0 = 1.3 \mu\text{m}$). The asterisks refer to dimensionless quantities; lines are just guides to the eyes (see text for details).

the bifurcation. This is further supported by a simple descriptive multipolar model of the force and torque maps, as shown in [10].

Figure 3 reveals that the structure of these maps also depends on the beam radius ω_0 . For a given $k > k_C$, the larger ω_0 , the weaker the forces and torques exerted on the particle. In turn, the dynamical response of the ellipsoid is perturbed in such a way that sustained oscillations may disappear (central and right panels in fig. 3). To recover the limit cycle, for instance for $\omega_0 = 2.6 \mu\text{m}$, one has to increase the aspect ratio up to ≈ 4.2 (recall that $k_C \cong 4.085$ for $\omega_0 = 1.3 \mu\text{m}$), so that the torque reaches a high enough value again whereas the force remains about the same. More generally, we found that the larger ω_0 , the higher k_C . This result confirms once again the major role of the torque in controlling the bifurcation towards the periodic attractor. It is illustrated more quantitatively in the graph of fig. 4, which shows the variations of the ratio $\rho = \Gamma_y^*/F_x^*$ (the asterisk refers to dimensionless quantities) as a function of the ellipsoid aspect ratio k . Γ_y^* (respectively F_x^*) is the maximum torque (respectively maximum force) encountered in the force-torque map for a given k . We see that ρ (blue symbols) grows steadily and monotonously with k , although it seems to level out a bit for $k > 4.5$. As supplementary information, the limit cycle area, A_{cycle}^* (black symbols), which could play the role of an order parameter by analogy to phase transitions, is also plotted in fig. 4. The cycle area seems to jump discontinuously from 0 to a finite value at k_C , indicating that the bifurcation is first order (sub-critical), as stated previously.

The above results undoubtedly show that the force and torque maps, computed as a function of both k and ω_0 , are of primary importance to understand the origin of sustained oscillations. Although we do not know the precise analytic form of the functions $F_x(x, \theta)$ and $\Gamma_y(x, \theta)$, the oscillations must arise from a *nonlinear* intertwining of these functions, which cannot be simply unveiled using handwaving arguments. For illustrative purposes, it may

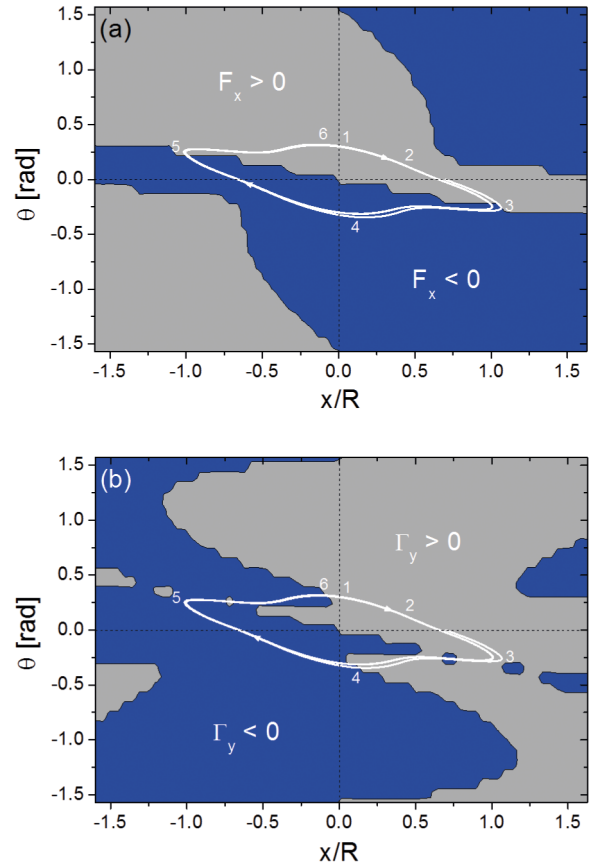


Fig. 5. Binary force (a) and torque (b) maps derived from fig. 3 (left part) where only the signs of F_x and Γ_y have been kept (*i.e.* +1 or -1). These maps better illustrate the regions where F_x and Γ_y change in sign. As in fig. 3, the limit cycle has been superimposed along with the same digits (see text for details).

be useful to superimpose the computed limit cycle with the corresponding force and torque maps, as shown in the left panel of fig. 3. The arrows indicate a clockwise cyclic motion whereas the digits 1, 2, 3, etc., marked along the cycle, represent different positions and orientations of the particle that we shall now briefly comment. In general, for $k > k_C$, sliding and/or tilting initially the particle in the positive quadrant ($x, \theta > 0$, point 1) results in the particle being expelled out of the beam because $F_x > 0$, *i.e.* the force is not restoring. The particle reaches a region where the torque is positive (point 2), making it rotate in a clockwise manner (with our convention). θ decreases and becomes negative. The particle now lies in a region ($x > 0, \theta < 0$) where the force has changed in sign and is restoring ($F_x < 0$, point 3). The particle is therefore brought back in the direction of the beam axis but the torque also changes in sign at point 4 ($\Gamma_y < 0$). Hence, x decreases while θ increases until the particle gets to point 5 where the force changes in sign again ($F_x > 0$). The particle is now pulled towards the $x > 0$ area, still with an increasing θ , till it reaches point 6 where the torque becomes positive. Then θ starts to decrease and the particle is driven back towards the positive quadrant where

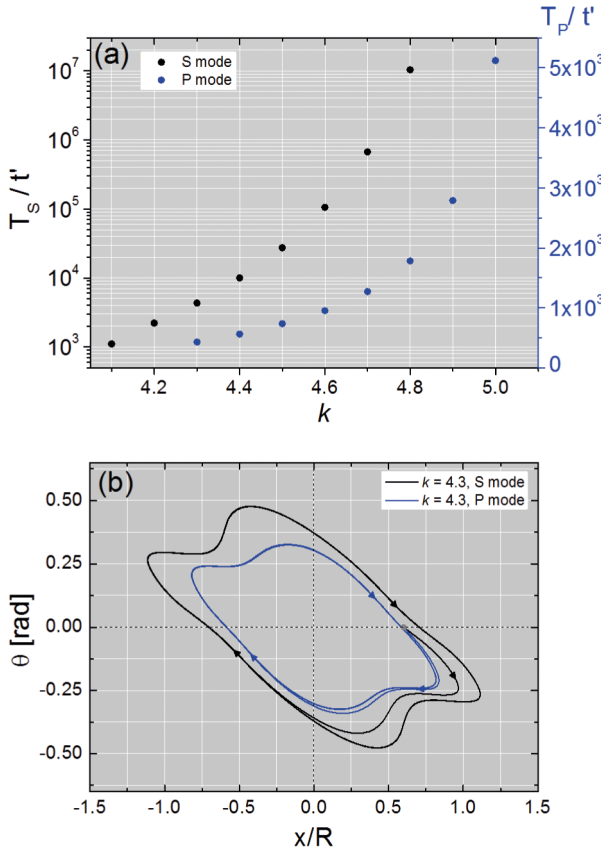


Fig. 6. (a) Computed period of the oscillations T (normalized by t') as a function of the aspect ratio k (with $k > k_C$) for the two polarization modes S and P (see text). (b) Evolution of the shape and size of the limit cycles as a function of the polarization mode. The grey dot indicates the starting conditions.

it started. This simple description gives an idea of how F_x and Γ_y couple in a subtle and peculiar way to produce permanent oscillations. But the general situation is actually more complicated since a variety of different maps can engender limit cycles, as we will see in the next section with focused beams.

It is instructive to re-plot the contour plots of fig. 3a,b (left part) using a binary color coding of the forces and torques where only the signs are kept (*i.e.* +1 or -1). In the resulting maps (see fig. 5), the regions where the force and torque change in sign are better resolved and appear as well-defined boundaries between different domains. As in fig. 3, the limit cycle has been superimposed and sign changes along the cycle can be easily spotted through a direct reading of crossed borders. We see that the force changes in sign at positions **3** and **5** while the torque does so at positions **4** and **6**, mainly. As described above, these sign changes are important to understand the origin of limit cycles. We will come back to this point in the discussion part.

The computed aspect ratio threshold k_C slightly depends on the beam polarization mode with $k_C(S) \approx 4.085$ and $k_C(P) \approx 4.275$ (with $\omega_0 = 1.3 \mu\text{m}$). At threshold, the

period of the oscillations, T , is smaller in the P mode (≈ 3.2 s) than in the S one (≈ 8.3 s) and both increase significantly —and even seem to diverge with k — as illustrated in fig. 6a. The increase is especially spectacular for the S mode, where T reaches values on the order of $\sim 10^4$ s, *i.e.* the system dynamics slows down dramatically. Correspondingly, the size of the associated limit cycles in the (x, θ) phase space increases with k for both polarization modes. However, due to slightly different force and torque values, the limit cycle in the P mode is always smaller than that in the S mode for a given k , as displayed in fig. 6b. In the latter case, the ellipsoid performs greater translational and rotational excursions from the beam axis and thus explores more remote areas where the forces and torques reach rather small values. It therefore takes more time to go around the cycle in this case. This might explain the different dynamics of the two modes.

Experimentally, the oscillating ellipsoids also perform motions well outside the beam axis but the beam polarization, be it linear in the S or P mode, or circular, does not influence the oscillation frequency, as already reported [11, 12]. Furthermore, the slowing down of the particle dynamics upon increasing k was not clearly evidenced in the experiments. We shortly comment on this point in the discussion part.

3.2 Focused beam

We shall now consider a focused laser beam with the aim of simulating the spreading of the actual laser beam due to diffraction. As aforesaid, the beam waist in the experiments is indeed small enough ($\omega_0 \approx 1.3 \mu\text{m}$) for diffraction effects to occur on the scale of particles lengths ($\approx 15 \mu\text{m}$). We then wish to investigate how the convergence/divergence of the incoming laser beam alters the ellipsoid dynamical state. One of the main consequences is that the system is no longer z -invariant and the altitude of the ellipsoid center of mass, z , with respect to the beam waist plane (fixed at $z = 0$), will now matter.

We conducted numerous dynamical calculations (integration of eqs. (11), (12)) as a function of both k and z . As before, the particle is again supposedly in contact to the top surface of the sample cell, and therefore only two degrees of freedom are considered (x and θ). Figure 7 summarizes the results in the form of state diagrams in the (k, z) -plane. The beam divergence was set to 5.4° which is equivalent, in the far field, to that of a Gaussian beam with a beam waist equal to $1.3 \mu\text{m}$. $z > 0$ ($z < 0$) means that the particle center of mass is located above (below) the $z = 0$ plane, respectively. In the former (latter) case, a diverging (converging) beam strikes the ellipsoid, respectively (see fig. 7a).

As a generalization of the conclusion drawn for collimated beams, we find that, for a given beam angle, sustained oscillations (blue points, fig. 7b,c) also appear only above a well-defined aspect ratio (here, $k_C \approx 3.65$ for $z = 0$ and S polarization mode). But, as expected, the

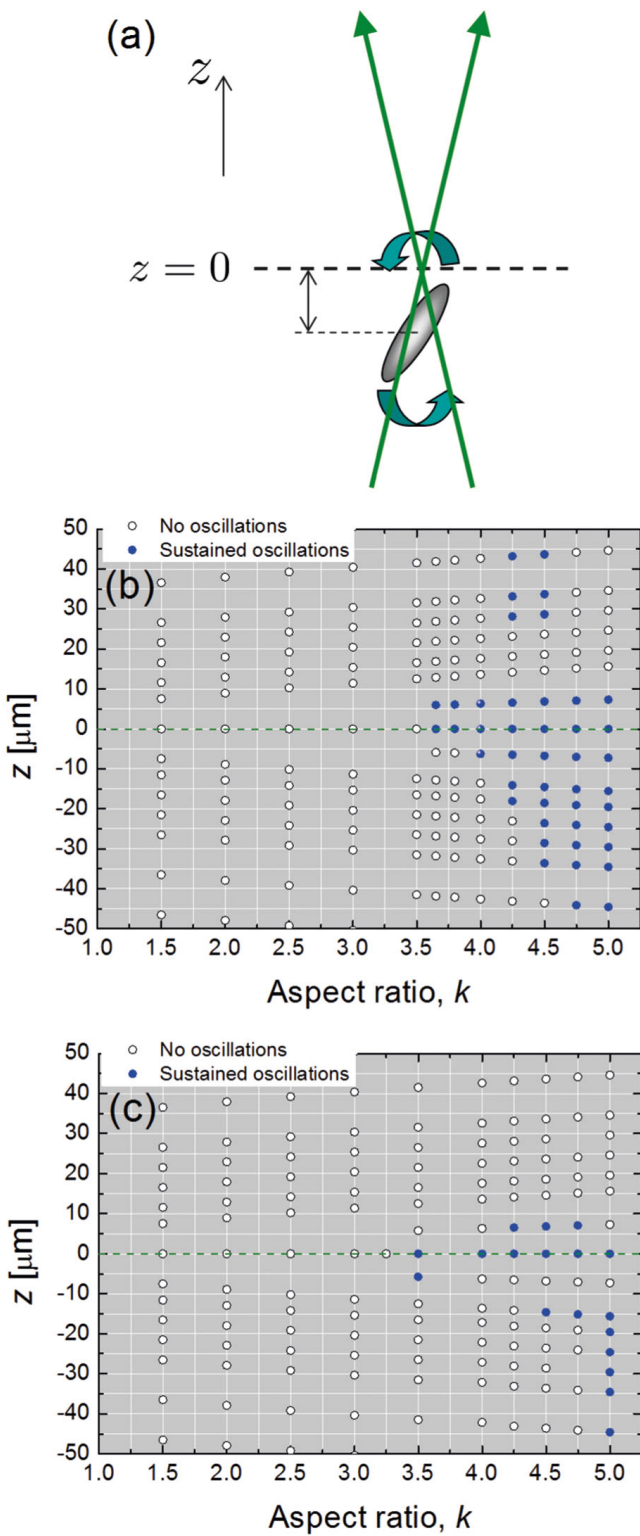


Fig. 7. (a) Schematic of our model focused beam (see subsect. 2.1 for details). (b), (c) State diagrams in the (k, z) -plane displaying the static (white circles) and dynamic (blue circles) stationary states of the ellipsoid for two different values of θ_D (5.4° in (b) and 10.023° in (c)). The beam converges (diverges) for $z < 0$ ($z > 0$), respectively. (S polarization mode).

ellipsoid dynamical state greatly depends on z , and furthermore, the $z \Leftrightarrow -z$ symmetry is broken since more oscillating states occur in the $z < 0$ region than in the $z > 0$ one. The latter fact is actually not too surprising since the rays of a converging beam will strike the particle surface at different locations than the rays of a diverging beam, thereby imparting different RP forces and torques to the particle and leading to different dynamics as well. Otherwise stated, $z < 0$ and $z > 0$ are qualitatively different situations, because they correspond to opposite signs in wave curvature with an actual laser beam. The greater $|z|$, the slower the particle dynamics because the particle is no longer exposed to the beam high intensity areas. For $k = 4.25$ and $z = +80 \mu\text{m}$, the particle even stops oscillating and reaches a static equilibrium at the $(x = 0, \theta = 0)$ point in a vertical position. This is reminiscent of the experimental observation mentioned in [10] where the oscillations are “killed” at large $|z|$, i.e. when the beam width becomes larger than, or comparable to, the ellipsoid (large) size. However, the observed horizontal flipping (see fig. 16 in [10]) is not seen in the calculations mainly because of the small tilt angle approximation used throughout (see eqs. (11), (12)).

Increasing the value of θ_D leads to the diagram exhibited in fig. 7c. Much fewer oscillating states occur in that case and most of them are located in the $z < 0$ region, i.e. with the ellipsoid located upstream the beam focus. This result would suggest that the use of tightly focused beams may help get rid of the oscillations although it could not be checked experimentally yet.

Depending on $|z|$ and k (with $k > k_C$), the origin $(0, 0)$ may be either a stable point attractor for small excursions of the ellipsoid, or conversely, an unstable one. In the latter situation, the particle is rejected from the beam center and either joins an outside limit cycle or simply drifts away from the beam axis without oscillating, in slow motion as the forces and torques get smaller and smaller. Occasionally though, two limit cycles show up: a small one encircling the origin in close proximity, and a bigger one located further away from it, as shown in fig. 8a. The two periodic attractors coexist and the ellipsoid bifurcates between them depending on the initial conditions. Figures 8b,c display the corresponding force and torque maps for that particular example. Note that the main features of these maps differ somewhat from those outlined in the case of a collimated beam (figs. 2, 3): the regions where the forces and torques change in sign differ and the locations where F_x and Γ_y are the most intense have evolved as well. This is not too surprising since the beam characteristics are not the same but, more importantly, it shows that different force and torque landscapes may lead to limit cycles and that there is not a unique one-to-one correlation between them. A systematic computation of the force and torque maps for all the points plotted in fig. 7 further supports this conclusion. Additional important comments about force and torque maps will be presented in the discussion part.

We shall now briefly mention the case of an ellipsoid put away from any boundary and no longer constrained

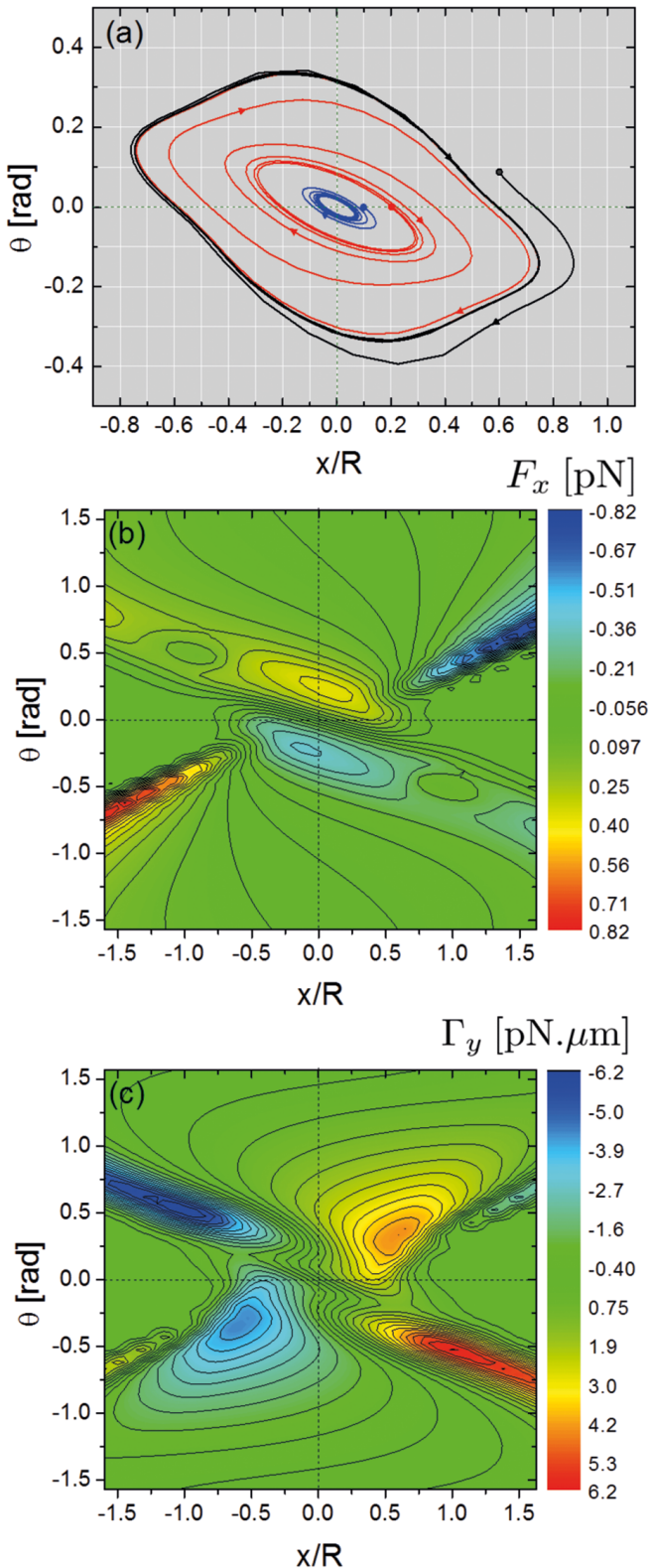


Fig. 8. (a) Coexistence of two limit cycles in phase space for $z = -14.119 \mu\text{m}$. Two trajectories (black and red curves) converge towards the larger limit cycle whereas the blue trajectory ends up on the smaller one. (b) and (c) show the corresponding contour plots for the force F_x and torque Γ_y , respectively ($\theta_D = 5.4^\circ$, $k = 4.25$).

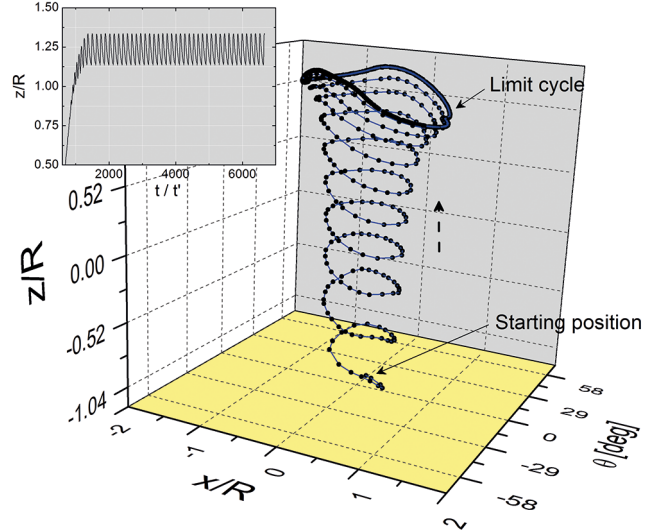


Fig. 9. Typical limit cycle obtained in a three-dimensional phase space after integration of eqs. (8), (9), (10). The laser beam propagates in the z -direction and the starting coordinates of the ellipsoid were ($x_0/R = 0$, $z_0/R \approx -1.2$, $\theta_0 = 10^\circ$) ($\theta_D = 5.4^\circ$, $k = 3.65$). Inset graph: Time evolution of the ellipsoid's altitude. The latter oscillates with an amplitude of about 0.2.

to be in contact to a solid wall. The buoyant weight of the particle is therefore balanced by the vertical component of the RP force and eqs. (8), (9), (10) are the relevant equations to be integrated to access the particle dynamics, still in the small tilt angle approximation. The particle can now move up and down in the z -direction. Dealing here with three degrees of freedom, x , z and θ , irregular or chaotic dynamics could be expected in addition to the previously encountered periodic motions in a two-dimensional phase space [56,57]. However, as far as dynamic stationary states are concerned, only limit cycles could be evidenced so far upon testing a few starting conditions and different aspect ratios. Figure 9 exhibits a typical limit cycle obtained in the three-dimensional phase space (x, z, θ) . Starting below the $z = 0$ plane, the ellipsoid is first pushed upwards whilst performing both translations and rotations. It then stabilizes in the $z > 0$ region where it oscillates in a periodic manner. The particle not only performs oscillations in x and θ but also in z as shown in the inset plot; however, the amplitude of the oscillations, of about $1 \mu\text{m}$, is too small to be clearly visible on the 3d trajectory. Although appealing, we should however consider the above result with some care since the substantial angular excursions of the ellipsoid ($\theta_{\max} \approx 50^\circ$, see fig. 9) largely break the small tilt angle approximation we used throughout up to now. Note that θ values as large as $\approx 25^\circ$ were already achieved in fig. 6b. However, we did test on some examples more general equations of motion not restricted to small tilt angles. Although the shape of limit cycles changes a bit, together with the values of x_{\max} and θ_{\max} , we found no major qualitative differences when compared to the solutions derived from the approximate equations (eqs. (8),

(9), (10) and eqs. (11), (12)). Thus, we believe that our results are meaningful and the data displayed in fig. 9 reinforces the general character of the oscillations due to RP forces, be the ellipsoid in contact to boundaries or located away from them.

4 Two coaxial beams

In this last section, we want to report a few results obtained with an ellipsoid illuminated by two coaxial counterpropagating beams. The latter configuration is a well-known solution to build a stable 3-dimensional optical trap when a long working distance is required (see, *e.g.*, [6, 58–60]). Our motivation here is to see if we can suppress the permanent oscillations for an ellipsoid with $k > k_C$. Achieving static equilibria of large- k ellipsoids indeed is necessary in basic levitation experiments where optical forces and torques are to be measured. The same requirement more generally holds in technological applications when oscillations of optically manipulated particles are undesirable.

Here we only consider the simplest case of two collimated beams, of same power, *i.e.* $P_T^{\text{down}} = P_T^{\text{up}}$. Then the forces and torques only depend on x and θ . We suppose that the forces and torques from both beams simply add incoherently (this condition is verified in experiments with spheres [61]). The total force and torque, $F^{(2)}$ and $\Gamma^{(2)}$, from *both* beams is obtained by linear superposition. Symmetry considerations derived from the force and torque maps obtained with a single beam lead to

$$F^{(2)}(x, \theta) = F^{(1)}(x, \theta) - F^{(1)}(-x, \theta), \quad (13)$$

$$\Gamma^{(2)}(x, \theta) = \Gamma^{(1)}(x, \theta) + \Gamma^{(1)}(-x, \theta), \quad (14)$$

where $F^{(1)}$ and $\Gamma^{(1)}$ are the force and torque from the upwards directed beam (see fig. 3). A fixed point (x_0, θ_0) , meaning a static configuration of the particle, then verifies

$$F^{(1)}(x_0, \theta_0) = F^{(1)}(-x_0, \theta_0) \quad (15)$$

and

$$\Gamma^{(1)}(x_0, \theta_0) = -\Gamma^{(1)}(-x_0, \theta_0). \quad (16)$$

Symmetry further indicates that mirror images of (x_0, θ_0) through x and θ axes are fixed points too, *i.e.* we obtain a quadruplet of fixed points: $(\pm x_0, \pm \theta_0)$.

The 2-beam simulation was carried out for an ellipsoid with $k = 4.1$, which is slightly above the aspect ratio threshold for oscillations in the one-beam levitation scheme. The results show that the particle no longer oscillates permanently in this case. Indeed, instead of limit cycles, the phase portrait of fig. 10a features a saddle-type instability at the origin with 4 stable fixed points located away from it and symmetrically distributed, as anticipated. Starting from diverse initial conditions, we find that the ellipsoid eventually immobilizes onto one of the fixed points after a few damped oscillations. The 2-beam arrangement then clearly “kills” the oscillations

seen in one-beam levitation. Note that the fixed points are located away from the x and θ axes, meaning that they correspond to oblique configurations: the particle is slightly off the laser beam axis and tilted (see side sketch in fig. 10a). The corresponding force and torque maps of this non-trivial situation are exhibited in figs. 10b,c. One can see that they have become quite symmetrical and comply with the anticipated symmetry relations stated above (eqs. (13), (14)).

In the previously discussed symmetrical scheme, the power ratio of the downwards directed beam to that of the up beam, $\rho = P_T^{\text{down}}/P_T^{\text{up}}$, was simply equal to 1. We shortly explored the effect of varying ρ , between 0 (one-beam scheme) and 1, still for $k = 4.1$. We found that oscillations were still present at $\rho = 0.1$, but were absent at $\rho = 0.5$. So the power ratio becomes the bifurcation control parameter in the two-beam scheme, for given particle characteristics. This conclusion is of direct practical interest, since ρ can be easily controlled in experiments.

5 Discussion and conclusion

In this paper, we have presented numerical calculations of the mechanical effects of light on transparent ellipsoidal particles. We used a simple 2-dimensional model based on ray-optics to compute the RP forces and torques exerted on the object as a function of position and orientation within the laser beam. Integration of the equations of motion, written in the small tilt angle approximation and in the Stokes limit, yields the particle dynamics that we investigated for different ellipsoid aspect ratios. The simulations predict that, above a critical aspect ratio k_C , the ellipsoid cannot be stably trapped; the particle instead permanently oscillates in a back-and-forth motion involving both translation and rotation in the vicinity of the beam axis. Conversely, the particle remains stably trapped on axis in a vertical position for $k < k_C$. This general result holds for both collimated and focused beams and is in excellent qualitative agreement with the experimental observations [10, 11]. A key point is that the oscillations can be accounted for by RP forces and torques alone, which is a further evidence of their non-conservative character [48, 62–65].

It is important to note that our simulation does not include a Langevin noise term, as it would be required if we were to explore characteristics of the particle’s Brownian motion. Neglecting the role of thermal fluctuations is practically justified by the fact that the present study mainly aims at understanding experiments carried out with large particles [10–12]. Here “large” means that ellipsoids used in experiments [10–12] were typically a few tens of micrometers in length. Brownian motion of such particles is visible under the microscope, but is very weak compared to the amplitudes of their cyclic motions, both in translation and rotation. It is then expectable that Brownian noise does not play a critical role in observed cyclic trajectories.

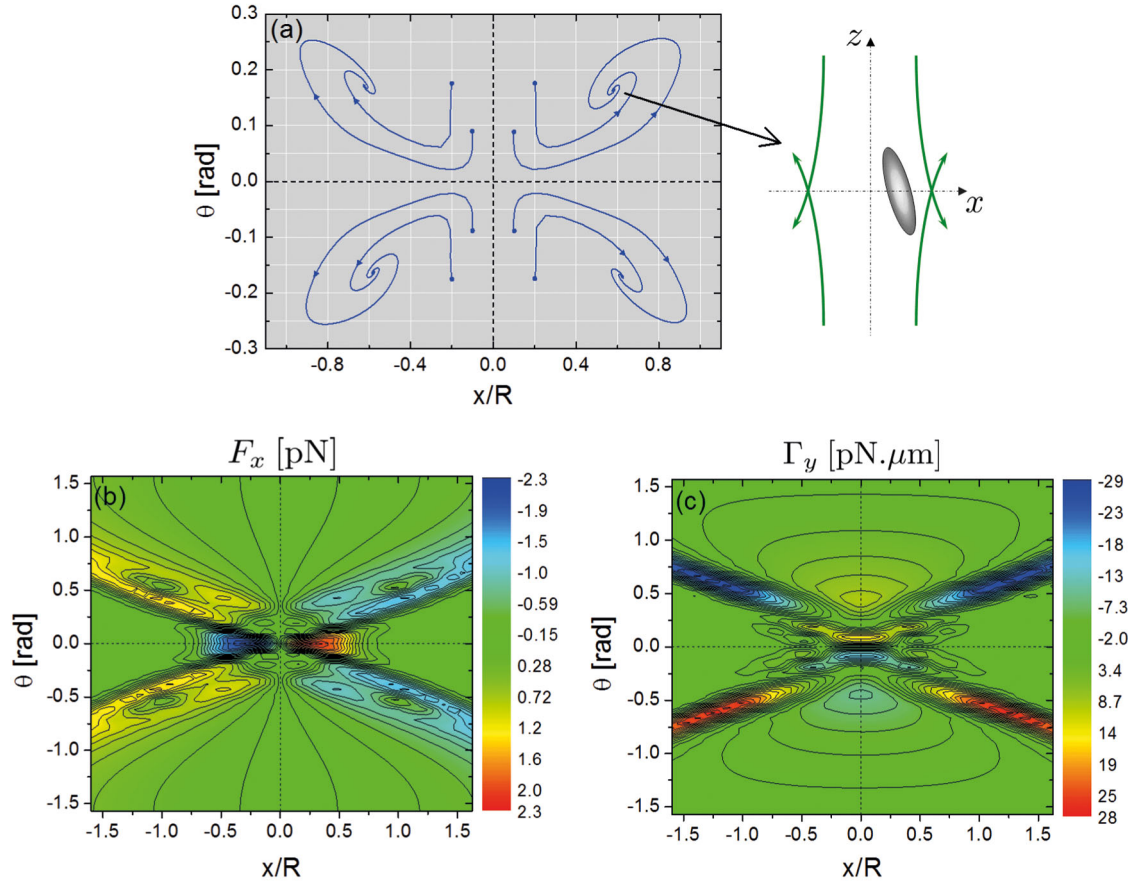


Fig. 10. Case of an ellipsoid illuminated by two coaxial counterpropagating collimated beams with equal powers. (a) Computed phase portrait showing a few phase trajectories converging on four-point attractors (fixed points) symmetrically located away from the origin (see sketch at right). The blue dots indicate the starting coordinates. The maps in (b) and (c) show the corresponding contour plots for the force F_x and torque Γ_y , respectively (beam radius $\omega_0 = 1.3 \mu\text{m}$, $k = 4.1$).

Most interestingly, Brownian motions of rod-like particles in single-beam gradient traps have been thoroughly studied in a recent theoretical work by Simpson and Hanna [62]. These authors explored the characteristics of thermally driven fluctuations of such particles close to the on-axis configuration ($x = 0$, $\theta = 0$) so that F and Γ can be approximated as linear functions of x and θ . They showed that the corresponding “stiffness matrix” \mathbf{K} was not symmetrical, meaning that the coupling of translations to torques is not equivalent to the coupling of rotations to forces. The latter property leads to cyclic motions of the particle around the $(0, 0)$ reference configuration. In this context, such motions were termed “first-order”, as they only involved the linear limit of the force-torque field. The profound reason for the existence of such motions, as explained in [62], is the asymmetry of the \mathbf{K} matrix, which is due to the non-conservative character of the optical force.

The oscillations of interest in our experiments [10] and in the present simulations are very different in nature from the aforementioned cyclic Brownian excursions. The difference is twofold: i) Brownian fluctuations only exist as a consequence of a Langevin noise source, which allows

the particle to explore the characteristics of the non conservative force-torque field. Thermal energy is absent in our simulation, and is likely to play a negligible role in the experiments with large-size ellipsoids. ii) The cyclic trajectories in our 2d model clearly lie in the non-linear domain of the force-torque maps, meaning that they are the consequence of the non-linear dependence of F and Γ to x and θ .

In a simplified reading of the numerical force-torque maps [10], meaning that we only retain the main features of the maps, the bifurcation seen in the 2d model turns out continuous (of super-critical Hopf type) and happens when the $(x = 0, \theta = 0)$ configuration becomes linearly unstable. Due to the latter (linear) instability, the particle gets ejected from the on-axis configuration. The linear approximation, in this context, soon becomes unphysical as it should drive the particle infinitely far (in x , say) from the axis. In reality, particle ejection saturates due to the non-linearities of F and Γ in x and θ . The latter non-linearities keep the particle at finite distance in the (x, θ) -plane. As the system is two-dimensional, the trajectory converges to a limit cycle [56, 57].

The latter analysis and conclusion hold even if fine details of the force-torque maps are taken into account. The main difference from the above-mentioned “simplified reading” lies in the fine structures of the maps close to $(x = 0, \theta = 0)$. In the simple case of a collimated beam, and for k slightly above k_C , these structures in fact do play a role for they maintain the origin point $(x = 0, \theta = 0)$ as a stable fixed point, in coexistence with the limit cycle. The stability of $(x = 0, \theta = 0)$ is however limited to a narrow domain ($x/R < 0.4, \theta < 10^\circ$), outside of which the fine structure does not significantly influence the particle’s dynamics.

We now wish to raise an important point about the binary maps displayed in fig. 5. On these (x, θ) maps, it is seen that the forces and torques change in sign at different locations, *i.e.* sign changes are shifted. We observed similar shifts by analyzing a few other maps featuring limit cycles and obtained with both a collimated and a focused beam. In fact, it turns out that this shift is very important to understand the origin of oscillations for we can show that it is a necessary (but not sufficient) condition for them to occur. A general proof of this property may be worked out if we consider that the limit cycle resulting from the full non-linear dynamical system, originates from an instability obtained at the linear limit of the system of equations.

The above valuable information allows us to state more clearly the necessary and sufficient conditions for the occurrence of permanent oscillations: i) existence of a shift in the sign changes of the force and torque fields and ii) the torque acting on the ellipsoid must be high enough. The latter condition is equivalent to reaching a threshold for the ellipsoid aspect ratio, as we saw above (see fig. 4). In particular, we checked that, the small limit cycle evidenced nearby the origin in fig. 8a fulfills condition i) above. It is also worth mentioning here that the previous conditions i) and ii), are consistent with the conclusions derived from the multipolar model worked out in Part I [10]. In this model, the shift between the force and torque poles, and their respective sign changes, is related to the parameter u . It was shown that if $u = 0$, the control parameter of the instability, A , diverges to infinity and, consequently, the bifurcation towards a limit cycle does not occur. Hence, $u > 0$ is a necessary condition for the oscillations to occur in this model as well.

As we saw, the way the RP forces and torques are coupled may be understood from the computed $F(x, \theta)$ and $\Gamma(x, \theta)$ maps whose structures greatly depend on k and the beam radius (ω_0). In particular, the torque amplitude seems to be the driving parameter of the instability. With a focused beam, the particle altitude z intervenes as a third parameter in the (F, Γ) maps. Calculated state diagrams in the (k, z) plane show that increasing the beam divergence tends to minimize the appearance of oscillations, and that these only exist if the particle centre is close enough to the beam focus. Oscillations are predicted to preferably occur for $z < 0$ when the beam aperture becomes large. Extrapolating to single-beam optical tweezers, the simulation then suggests that sustained oscillations

only exist when the particle is maintained below the laser focus. The latter condition may be met by pushing the particle against the top interface of the sample cell, as in [18].

While particle oscillations bear their own academic interest and have potential applications as a micro-motor, they rather come as a problem in situations where particle static equilibrium is desirable. We shortly explored the possibility of “killing” oscillations through the use of a couple of counterpropagating beams architecture. We indeed verified that a downward directed beam was able to suppress the oscillations, with the consequence of the ellipsoidal particle lying in an oblique and slightly off-centred configuration. This point is to be verified in forthcoming experiments.

The 2d ray-optics model helped us understand key features of experimentally observed particle dynamics and was able to make some likely predictions, but it obviously has severe limitations. These mainly stem from the ray-optics approximation itself, which is a crude representation of a laser beam and completely ignores wave effects in the laser-particle interaction. Moreover, restriction to dimension 2 obviously misses the role of out-of-plane reflections and refractions, which are unimportant with spheres but may have a great influence with ellipsoids.

Due to these limitations, the model can only make qualitative predictions. The value of the bifurcation parameter (*e.g.*, $k \approx 3.6$ in fig. 7) is not far from that experimentally obtained with $\omega_0 = 1.3 \mu\text{m}$. However, the calculated value depends on the laser polarization state, while the latter has about no influence in experimental records [10]. Dependence on the polarization is clearly a weakness of the 2d representation. In experiments, oscillating particles undergo 3d motions around the beam axis, which probably mask polarization characteristics of the beam.

Another disagreement, whose cause is less obvious, is about the period of particle oscillations as k increases. As can be seen in fig. 6a, calculated T values divergently increase when k is varied between 4 and 5, while no clear-cut trend could be inferred from the experimental measurements [10]. The 2d character of our model is again perhaps subject to questions on this issue.

In spite of the limitations inherent to ray-optics, there is still much to learn through a generalization of the model to three dimensions. The third dimension intervenes through rays that propagate out of plane, the first step in upgrading the simulation, but also in the particle shape itself. Indeed particles in experiments are most often not spheroids (*i.e.* are not cylindrically symmetrical) but have three different axes lengths. This lack of symmetry may be the source of irregular dynamics, as seen in [10].

A more general formulation of the equations of motion in 3 dimensions, not limited to small angular excursions, should also be worked out. Finally, it may be worth studying as well the influence of thermal fluctuations on the particle dynamics. Though Brownian noise probably has a negligible influence on limit cycles, it may have some very

close to the bifurcation threshold. This statement holds for large size ellipsoids, as aforesaid. Conversely, Brownian motion expectably has a much greater influence and may substantially alter the dynamics of very small particles, such as nanowires, nanotubes or other nanometer-sized objects used in the nanotechnology industry [31].

We acknowledge financial support from the French government through the “AMOCOPS” project (2013–2017) of Agence Nationale de la Recherche (ANR-13-BS09-008), the Conseil Régional d’Aquitaine and the ITN-COMPLOIDS (2009–2013) European network. The authors thank J. Elezgaray, F. Ren, and J.-P. Galaup for stimulating discussions and are grateful to the laboratory computer service for its assistance.

Appendix A. Expression of the effective length \tilde{R}

We consider an ellipsoid such as in fig. 11. a and b are the long and short semi-axis lengths, respectively, and k is the aspect ratio. The particle centre is denoted C , of coordinates (x, z) in the (O, x, z) frame.

In the Stokes regime, the equation for the torque acting on the particle reads

$$\boldsymbol{\Gamma}_{\text{op}C} + \boldsymbol{\Gamma}_{\text{h}C} + \boldsymbol{\Gamma}_{\text{LC}} = 0, \quad (\text{A.1})$$

where $\boldsymbol{\Gamma}_{\text{op}C}$ is the torque due to optical forces, $\boldsymbol{\Gamma}_{\text{h}C}$ the hydrodynamic torque, and $\boldsymbol{\Gamma}_{\text{LC}}$ is the torque due to the contact of the particle on the top surface. In the small angle approximation

$$\boldsymbol{\Gamma}_{\text{LC}} = \tilde{R} \theta \mathbf{F} \cdot \hat{\mathbf{z}}, \quad \text{with} \quad \tilde{R} = R k^{-4/3} (k^2 - 1), \quad (\text{A.2})$$

as written in eq. (12). We will now justify eq. (A.2).

The contact point of the ellipsoid on the top surface is denoted A in fig. 11. We suppose that contact to the interface has no influence on hydrodynamic dissipation. The interface reaction is then simply a vertical force \mathbf{L} which balances the vertical component of the optical force: $\mathbf{L} = -F_z \hat{\mathbf{z}}$ (with $F_z = \mathbf{F} \cdot \hat{\mathbf{z}}$). The corresponding torque is $\boldsymbol{\Gamma}_{\text{LC}} = \mathbf{CA} \times \mathbf{L}$.

We calculate the coordinates (X_A, Z_A) of A in the (C, X, Z) frame (see fig. 11). (X_A, Z_A) is the solution of the couple of equations

$$f(X, Z) = 0, \quad (\text{A.3})$$

$$\frac{\partial f(X, Z)}{\partial x} = 0, \quad (\text{A.4})$$

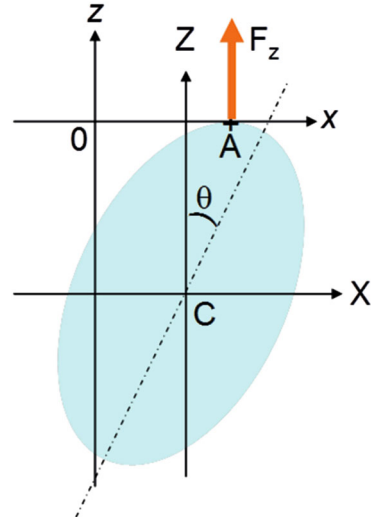


Fig. 11. Geometry used for the derivation of eq. (A.2) (see appendix A).

with

$$f(X, Z) = \frac{(Z \cos \theta + X \sin \theta)^2}{a^2} + \frac{(-Z \sin \theta + X \cos \theta)^2}{b^2} - 1. \quad (\text{A.5})$$

The explicit form of eq. (A.4) now reads

$$\sin \theta \frac{(Z \cos \theta + X \sin \theta)}{a^2} + \cos \theta \frac{(-Z \sin \theta + X \cos \theta)}{b^2} = 0. \quad (\text{A.6})$$

Solving for (X, Z) in eqs. (A.5), (A.6) is straightforward. We obtain

$$\mathbf{CA} = \begin{pmatrix} \sin \theta \cos \theta \frac{a^2 - b^2}{\sqrt{a^2 \cos^2 \theta + b^2 \sin^2 \theta}} \\ -z \end{pmatrix}. \quad (\text{A.7})$$

Since the ellipsoid has the same volume as the mother sphere of radius R , we have $R^3 = ab^2 = kb^3$. Then

$$\mathbf{CA} = \begin{pmatrix} R \sin \theta \cos \theta \frac{k^{-1/3} (k^2 - 1)}{\sqrt{k^2 \cos^2 \theta + \sin^2 \theta}} \\ -z \end{pmatrix}. \quad (\text{A.8})$$

To first order in θ , eq. (A.8) yields

$$\mathbf{CA} \cong \begin{pmatrix} R \theta k^{-4/3} (k^2 - 1) \\ -z \end{pmatrix}, \quad (\text{A.9})$$

leading to eq. (A.2) above. Note that $\boldsymbol{\Gamma}_{\text{LC}} = 0$ for a sphere ($k = 1$). In this case, A and C lie on the same vertical and the contact force does not contribute to the torque.

References

1. E.F. Nichols, G.F. Hull, Phys. Rev. **13**, 307 (1901).
2. P. Lebedev, Ann. Phys. **6**, 433 (1901).
3. A. Ashkin, Phys. Rev. Lett. **24**, 156 (1970).
4. A. Ashkin *et al.*, Opt. Lett. **11**, 288 (1986).
5. A. Ashkin, *Optical trapping and manipulation of neutral particles using lasers* (World Scientific, London, 2006).
6. G. Roosen, C. Imbert, Phys. Lett. A **59**, 6 (1976).
7. S. Chu, Rev. Mod. Phys. **70**, 685 (1998).
8. C. Cohen-Tannoudji, Rev. Mod. Phys. **70**, 707 (1998).
9. Phillips, Rev. Mod. Phys. **70**, 721 (1998).
10. B.M. Mihiretie, P. Snabre, J.-C. Loudet, B. Pouliquen, Eur. Phys. J. E **37**, 124 (2014).
11. B.M. Mihiretie, P. Snabre, J.-C. Loudet, B. Pouliquen, EPL **100**, 48005 (2012).
12. B. Mihiretie, J.-C. Loudet, B. Pouliquen, J. Quantum Spectrosc. Radiat. Transfer **126**, 61 (2013).
13. J.N. Wilking, T.G. Mason, EPL **81**, 58005 (2008).
14. A. Jonáš, P. Zemánek, Electrophoresis **29**, 4813 (2008).
15. K. Dholokia, T. Čižmár, Nat. Photon. **5**, 335 (2011).
16. P.J. Pauzauskie *et al.*, Nat. Mater. **5**, 97 (2006).
17. A. Neves *et al.*, Opt. Express **18**, 822 (2010).
18. Z. Cheng, P.M. Chaikin, T.G. Mason, Phys. Rev. Lett. **89**, 108303 (2002).
19. Z. Cheng, T.G. Mason, P.M. Chaikin, Phys. Rev. E **68**, 051404 (2003).
20. S.H. Simpson, S. Hanna, J. Opt. Soc. Am. A **27**, 1255 (2010).
21. Y. Cao *et al.*, Opt. Express **20**, 12987 (2012).
22. R.C. Gauthier, J. Opt. Soc. Am. B **14**, 3323 (1997).
23. R.C. Gauthier, M. Ashman, C.P. Grover, Appl. Opt. **38**, 4861 (1999).
24. P.B. Bareil, Y. Sheng, Opt. Express **18**, 26388 (2010).
25. S.H. Simpson, S. Hanna, J. Opt. Soc. Am. A **28**, 850 (2011).
26. S.H. Simpson, S. Hanna, J. Opt. Soc. Am. A **24**, 430 (2007).
27. S.H. Simpson, S. Hanna, Phys. Rev. A **84**, 053808 (2011).
28. H. Sosa-Martínez, J.C. Gutiérrez-Vega, J. Opt. Soc. Am. B **26**, 2109 (2009).
29. C.B. Chang *et al.*, Opt. Express **20**, 24068 (2012).
30. A. Van der Horst *et al.*, Opt. Express **15**, 11629 (2007).
31. O.M. Maragò *et al.*, Nat. Nanotechno. **8**, 807 (2013).
32. A.S. Glassner, *An Introduction to Ray-Tracing* (Morgan Kaufmann, San Francisco, 1989).
33. J.D. Jackson, *Classical Electrodynamics* (John Wiley & Sons Ltd., 1975).
34. G. Gouesbet, B. Maheu, G. Grehan, J. Opt. Soc. Am. A **5**, 1427 (1988).
35. K.F. Ren, G. Grehan, G. Gouesbet, Opt. Commun. **108**, 343 (1994).
36. F. Xu *et al.*, Phys. Rev. E **75**, 026613 (2007).
37. B.T. Draine, P.J. Flatau, J. Opt. Soc. Am. A **11**, 1491 (1994).
38. P.C. Chaumet, A. Rahmani, M. Nieto-Vesperinas, Phys. Rev. Lett. **88**, 123601 (2002).
39. M.A. Yurkin, A.G. Hoekstra, J. Quantum Spectrosc. Radiat. Transfer **106**, 558 (2007).
40. D. Bonessi, K. Bonin, T. Walker, J. Opt. A: Pure Appl. Opt. **9**, S228 (2007).
41. D. Benito, S.H. Simpson, S. Hanna, Opt. Express **16**, 2942 (2008).
42. J.-Q. Qin *et al.*, Opt. Express **17**, 8407 (2009).
43. D.A. White, J. Comput. Phys. **159**, 13 (2000).
44. J.M. Song, W.C. Chew, Micro. Opt. Tech. Lett. **10**, 14 (1995).
45. X.Q. Sheng *et al.*, IEEE Trans. Antenn. Propag. **46**, 1718 (1998).
46. V.K. Varandan, V.V. Varandan (Editors), *Acoustic, Electromagnetic and Elastic Wave Scattering: Focus on the T-matrix Approach* (Pergamon, 1980).
47. T.A. Nieminen *et al.*, J. Opt. A: Pure Appl. Opt. **9**, S196 (2007).
48. A. Ashkin, J. Biophys. **61**, 569 (1992).
49. J.Y. Walz, D.C. Prieve, Langmuir **8**, 3073 (1992).
50. F. Xu *et al.*, Phys. Rev. A **78**, 013843 (2008).
51. A. Hinojosa-Alvarado, J.C. Gutiérrez-Vega, J. Opt. Soc. Am. B **27**, 1651 (2010).
52. J. Happel, H. Brenner, *Low Reynolds Number Hydrodynamics* (Kluwer, Dordrecht, 1991).
53. Y. Han *et al.*, Phys. Rev. E **80**, 011403 (2009).
54. W.H. Press, B.P. Flanery, S.A. Teukolsky, *Numerical Recipes* (Cambridge University Press, 1989).
55. J.H. Mathews, *Numerical Methods* (Prentice-Hall International, 1992).
56. R. Rosen, *Dynamical System Theory in Biology*, Vol. **1** (Wiley-Interscience, 1970).
57. J.M.T. Thompson, H.B. Stewart, *Nonlinear Dynamics and Chaos* (John Wiley & Sons, 1986).
58. P.J. Rodrigo, V.R. Daria, J. Glückstad, J. Opt. Lett. **29**, 2270 (2004).
59. P.J. Rodrigo, I.R. Perch-Nielsen, J. Glückstad, Opt. Express **14**, 5812 (2006).
60. P. Kraikivski, B. Pouliquen, R. Dimova, Rev. Sci. Instrum. **77**, 113703 (2006).
61. M.I. Angelova, B. Pouliquen, Pure Appl. Opt. **2**, 261 (1993).
62. S.H. Simpson, S. Hanna, Phys. Rev. E **82**, 031141 (2010).
63. Y. Roichman *et al.*, Phys. Rev. Lett. **101**, 128301 (2008).
64. B. Sun *et al.*, Phys. Rev. E **80**, 010401(R) (2009).
65. G. Pesce *et al.*, EPL **86**, 38002 (2009).